Wei Lin
School of Engineering Science,
University of Chinese Academy of Sciences,
Beijing 100049, China;
Institute of Porous Flow and Fluid Mechanics,
Chinese Academy of Sciences,
Langfang, Hebei 065007, China;
Department of Earth and Planetary Science,
University of California,
Berkeley, CA 94720;
Research Institute of Petroleum Exploration &
Development,
PetroChina Company Limited,
Beijing 100083, China
e-mail: ucaslinwei@126.com

Xizhe Li[1]
School of Engineering Science,
University of Chinese Academy of Sciences,
Beijing 100049, China;
Institute of Porous Flow and Fluid Mechanics,
Chinese Academy of Sciences,
Langfang, Hebei 065007, China;
Research Institute of Petroleum Exploration &
Development,
PetroChina Company Limited,
Beijing 100083, China
e-mail: lxz69@petrochina.com.cn

Zhengming Yang[1]
School of Engineering Science,
University of Chinese Academy of Sciences,
Beijing 100049, China;
Institute of Porous Flow and Fluid Mechanics,
Chinese Academy of Sciences,
Langfang, Hebei 065007, China;
Research Institute of Petroleum Exploration &
Development,
PetroChina Company Limited,
Beijing 100083, China
e-mail: yzhm69@petrochina.com.cn

Shengchun Xiong
School of Engineering Science,
University of Chinese Academy of Sciences,
Beijing 100049, China;
Institute of Porous Flow and Fluid Mechanics,
Chinese Academy of Sciences,
Langfang, Hebei 065007, China;
Research Institute of Petroleum Exploration &
Development,
PetroChina Company Limited,
Beijing 100083, China
e-mail: xiongshengchun@petrochina.com.cn

Modeling of 3D Rock Porous Media by Combining X-Ray CT and Markov Chain Monte Carlo

Rocks contain multi-scale pore structures, with dimensions ranging from nano- to sample-scale, the inherent tradeoff between imaging resolution and sample size limits the simultaneous characterization of macro-pores and micro-pores using single-resolution imaging. Here, we developed a new hybrid digital rock modeling approach to cope with this open challenge. We first used micron-CT to construct the 3D macro-pore digital rock of tight sandstone, then performed high-resolution SEM on the three orthogonal surfaces of sandstone sample, thus reconstructed the 3D micro-pore digital rock by Markov chain Monte Carlo (MCMC) method; finally, we superimposed the macro-pore and micro-pore digital rocks to achieve the integrated digital rock. Maximal ball algorithm was used to extract pore-network parameters of digital rocks, and numerical simulations were completed with Lattice-Boltzmann method (LBM). The results indicate that the integrated digital rock has anisotropy and good connectivity comparable with the real rock, and porosity, pore-throat parameters and intrinsic permeability from simulations agree well with the values acquired from experiments. In addition, the proposed approach improves the accuracy and scale of digital rock modeling and can deal with heterogeneous porous media with multi-scale pore-throat system. [DOI: 10.1115/1.4045461]

Keywords: digital rock, tight sandstone, X-ray CT, MCMC, LBM, oil/gas reservoirs, petroleum engineering, unconventional petroleum

[1]Corresponding authors.

Contributed by the Petroleum Division of ASME for publication in the JOURNAL OF ENERGY RESOURCES TECHNOLOGY. Manuscript received May 26, 2019; final manuscript received November 3, 2019; published online November 12, 2019. Assoc. Editor: Gensheng Li.

Yutian Luo
School of Engineering Science,
University of Chinese Academy of Sciences,
Beijing 100049, China;
Institute of Porous Flow and Fluid Mechanics,
Chinese Academy of Sciences,
Langfang, Hebei 065007, China;
Research Institute of Petroleum Exploration & Development,
PetroChina Company Limited,
Beijing 100083, China
e-mail: luoyutian@petrochina.com.cn

Xinli Zhao
School of Engineering Science,
University of Chinese Academy of Sciences,
Beijing 100049, China;
Institute of Porous Flow and Fluid Mechanics,
Chinese Academy of Sciences,
Langfang, Hebei 065007, China;
Research Institute of Petroleum Exploration & Development,
PetroChina Company Limited,
Beijing 100083, China
e-mail: zhaoxinli17@mails.ucas.edu.cn

1 Introduction

Geomaterials such as rocks and soils contain multiscale pore structures, with dimensions ranging from the nanometer to the sample-scale, and the full range of spatial scales can be challenging to characterize for natural samples. Because of the high cost and difficulty of coring, engineers and scientists usually use synthetic rocks such as cemented cores and sand-pack columns instead of natural rocks to perform control experiments on water, gas and oil seepage and determine solid mechanical properties. For instance, synthetic rocks have been used to study a variety of transport processes that occur during contaminant transport, sequestration of greenhouse gases, and enhanced oil/gas recovery. This includes groundwater contamination [1–3], immobilization of radioactive wastes [4], CO_2 storage [5,6], residual oil displacement during flooding [7,8], the effect of ionic liquids [9], and the role of pore geometry on diffusion and permeability [10]. However, natural rocks have additional structures such as microcracks in crystalline rocks, and sedimentary rocks typically contain voids in a variety of shapes, including nodal pores situated at grain vertices and sheet-like throats along two-grain boundaries [11]. Many literatures have documented such differences, Yin et al. [12] studied synthetic rock analog for permeability studies of rock salt with mudstone and found that the formation mechanisms of natural rock specimen and synthetic specimen were different; the porosity and permeability of synthetic specimens were similar to those of the natural specimens, but the natural rock (mudstone/salt) had different pore space structures compared with the synthetic specimens. Han et al. [13] conducted a comparative study on synthetic cores and natural cores and found that for samples with similar permeability, natural cores have more complex pore structures, lower connectivity, and stronger heterogeneity than synthetic cores. Consequently, laboratory simulation experiments using synthetic rocks are vulnerable to experimental errors and also difficult to achieve strict blank control.

Nowadays, digital rocks are becoming the optimal replicas of natural rocks. Digital rock technology originated in the 1970s and has developed into a critical tool in the field of rock physics. Compared with conventional petrophysical analysis methods, digital rocks have the following advantages [14–16]: (1) they ensure that the rocks can be used repeatedly and indefinitely; (2) they permit numerical simulation of physical and transport properties including fluid-solid coupling and multiphase flows; (3) they enable study of unconsolidated or fractured reservoir rocks that are difficult to sample; (4) they can be used to quantitatively study the influence of various microscopic properties (pore-throat structure, wettability, water-bearing film, etc.) on the macroscopic properties (permeability, conductivity, etc.). Digital rocks have enabled important breakthroughs in understanding how hydrocarbons enter pore spaces and the mechanisms of oil and gas seepage as well.

At present, there are three main methods to construct digital rocks: physical experiments, numerical reconstructions, and hybrid modeling. Physical experiment methods capture a large number of 2D images using various imaging tools such as an optical microscope, scanning electron microscope (SEM), and computed tomography (CT) scanner. Examples include serial section tomography (SSTM) [17], laser scanning confocal microscopy [18], and X-ray CT scanning [19,20]. A modeling program or software (e.g., AVIZO, DRAGONFLY, and IMAGE J) superimposes the 2D images to create 3D digital rocks. X-ray CT scanning is the most widely used and has the advantages of high accuracy and being nondestructive. The main disadvantage is that there is an inherent trade-off between the volume imaged and the resolution. Importantly, pores and throats smaller than the scanning resolution are unidentifiable, but these structures can have a large effect on transport and mechanical properties [21–24]. Unlike physical experiment methods, numerical reconstruction methods are usually based on a small number of 2D images, and use mathematical algorithms to construct 3D digital rocks. The numerical reconstruction methods can be divided into stochastic methods and process-based methods (PBM). Stochastic methods use statistical characteristics (e.g., porosity, pore size distribution, two-point cluster functions, and fractal system control functions) as the reconstruction constraint functions, with examples including the truncated Gaussian random field method (TGRFM) [25], simulated annealing method [26,27], multiple-point geostatistics method [28–30], sequential indicator simulation method [31], Markov chain Monte Carlo (MCMC) method [32–35], PBM reconstruct 3D digital rocks by simulating the formation process of sedimentary rocks including sedimentation and diagenesis [36,37]. The numerical reconstruction method has the advantages of relatively straightforward data acquisition, rapid

image processing, and wide applicability, and its drawback is that there is a difference between the built model and the real rock. Hybrid models can overcome some limitations of a single modeling method. For example, Talukdar and Torsaeter [38] used the TGRFM as an input for the simulated annealing method (SAM). Politis et al. [39] and Liu et al. [40] reconstructed 3D digital rocks by combining PBM and SAM, taking the output of PBM as the input of SAM; compared with the routine SAM, their hybrid numerical reconstruction methods are more efficient and accurate. Furthermore, Lin et al. [41] introduced a hybrid modeling method with a combination of physical experiments and numerical reconstruction. This method not only keeps the accuracy of the macro-pore image, but also contains microstructure information. In general, the hybrid methods have improved modeling accuracy and efficiency, avoiding many limitations of separate modeling method.

In this work, we developed a new hybrid modeling method for digital rocks. We employed micron-CT to image the macro-pore structure of tight sandstone and constructed the macro-pore digital rock, and used the SEM to characterize the micro-pore of tight sandstone and reconstructed the micro-pore digital rock using MCMC. We obtained the integrated digital rock of tight sandstone by the superposition of micro- and macro-pore digital rocks and comparatively analyzed rock physical properties and seepage characteristics. Compared with the hybrid modeling method proposed by Lin et al. [41], this method can establish a more accurate micro-pore digital rock since MCMC can capture more petrophysical information than SAM and take into account the heterogeneity and anisotropy of rocks, thus improving the accuracy of integrated digital rock.

2 Construction of 3D Digital Rocks of Tight Sandstone

2.1 3D Macro-Pore Digital Rock by X-Ray Computed Tomography. Tight sandstone has typical dual pore characteristics, showing the bimodal distribution on the nuclear magnetic resonance T2 spectrum. The short T2 time in the T2 spectrum represents the micro-pore space, and the long T2 time represents the macro-pore space [42–45]. This study employed UltraXRM-L200 CT scanner to image macro-pores (>1 μm) of the tight sandstone. The sandstone sample was made into the cylinder with approximately 1.0 mm diameter and 1.1 mm length; its porosity is 14.75% and gas permeability is 0.317×10^{-3} μm^2. The resolution of CT imaging is 1.0 μ/pixel, and 1014 CT grayscale images were obtained (as shown in Figure 1). The original grayscale images were preprocessed by contrast enhancement and non-local means filter. There are many grayscale image segmentation algorithms, such as iterative method [46], Otsu method [47], and simple statistical method [48]. We adopted a new improved threshold segmentation method considering pore fractal characteristics [49] to achieve the optimal segmentation. Figure 2 shows a binary image of tight sandstone for 3D modeling (white is solid and black is void). Figure 3 presents a 3D macro-pore digital rock obtained by processing CT images, whose physical size is 0.1 mm × 0.1 mm × 0.1 mm and voxel size is 100 × 100 × 100.

2.2 3D Micro-Pore Digital Rock by MCMC. We cut the rock cylinder scanned by CT into a small cube and used SEM to scan three orthogonal planes (i.e., XY, XZ, and YZ planes, and the XY planes of SEM images are parallel to the CT images), and this operation is intended to capture the heterogeneity and anisotropy of rocks. In order to capture the micro-pore characteristics of rock and reconstruct the micro-pore digital rock, we selected the subareas containing mainly micropores for SEM scanning and 3D reconstruction, as shown in Fig. 4. The resolution of SEM images is 0.25 micron/pixel, the same image processing used for the CT images was used to create the binary SEM images, as shown in Fig. 5.

Based on the binary SEM images of different planes, the 3D micro-pore digital rock was constructed by Markov Chain Monte Carlo method (MCMC) [32,33]. The basic principles are as follows:

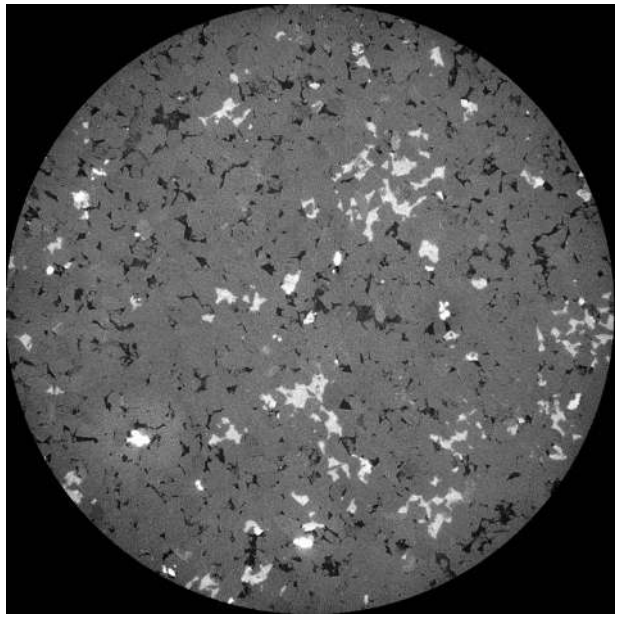

Fig. 1 CT grayscale image of core column (990 × 990 pixels)

For a particular point o, Λ_{-o} represents all points except o, so a neighbor N_o of o can be represented as

$$f(x_o|x(\Lambda_{-o})) \approx f(x_o|x(N_o)) \tag{1}$$

Assume $V_{LMN} = \{(l, m, n): 0 < l \le L, 0 < m \le M, 0 < n \le N\}$ represents a rectangular mesh with L rows, M columns, N layers of square voxels, (i, j, k) represents the intersecting voxels of row i, column j, and layer k, and its related state is expressed as X_{ijk}. V_{ijk} is a rectangular mesh with length i, width j, and height k, and its related state is $X(V_{ijk})$. According to the above equations, the conditional probability of the random Markov field for each voxel is

$$f(x_{ijk}|\{x_{lmn}:(l, m, n) \neq (i, j, k)\}) = f(x_{ijk}|\{x_{lmn}:(l, m, n) \in N(ijk)\}) \tag{2}$$

where $N(ijk)$ is a neighbor of (i, j, k).

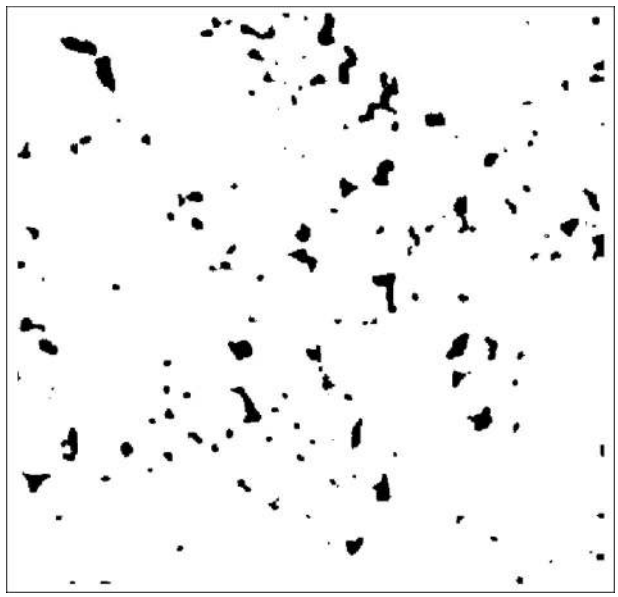

Fig. 2 Binary image of tight sandstone used for modeling (100 × 100 pixels, white is solid, and black is void)

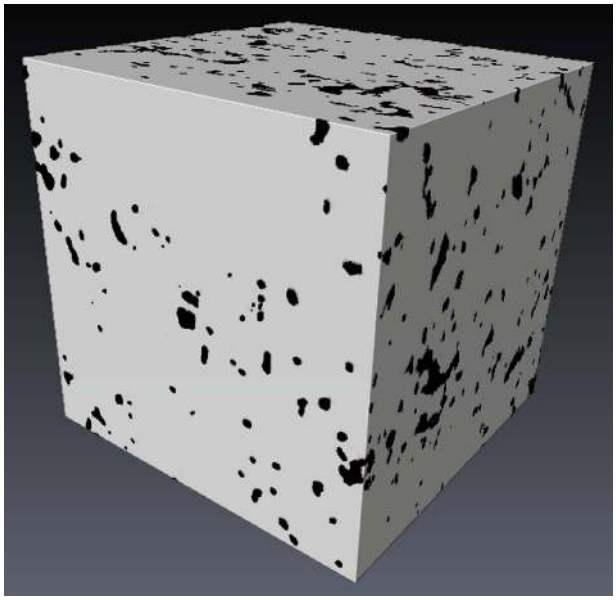

Fig. 3 3D macro-pore digital rock modeled using X-ray CT scanning method (gray is solid and black is void)

Based on the SEM binary images (void is labeled 0 and solid is labeled 1), three planes of XY, YZ, and XZ were used to construct the three-dimensional Markov chain model simultaneously.

Figure 6 exhibits the micro-pore digital rock which was constructed by the MCMC, whose physical size is 0.1 mm × 0.1 mm × 0.1 mm and the voxel size is 400 × 400 × 400.

2.3 Integrated Digital Rock. We used the superposition method [21,41] to integrate two digital rocks and superposed along the XY plane of the models. According to the resolution ratio of macro-pore digital rock to micro-pore digital rock i ($i = 4$), the voxels of macro-pore digital rock were divided into $i \times i \times i$ voxels. The voxel refinement diagram is shown in Fig. 7.

The pores of both digital rocks are superimposed, and the superimposed pores I_S are

$$I_S = I_A \cup I_B \tag{3}$$

where I_A and I_B represent the pore space of macro-pore digital rock and micro-pore digital rock, respectively. Given that the void pixels and solid pixels of the binary image are characterized by 0 and 1, respectively, the superposition operation is

$$0_A + 0_B = 0_S, \quad 0_A + 1_B = 0_S, \quad 1_A + 0_B = 0_S, \quad 1_A + 1_B = 1_S \tag{4}$$

We note that by imposing "$1_A + 0_B = 0_S$", the algorithm creates a positive bias for the void pixels, where we assume that the pixels identified as void at low resolution are always void pixels at high resolution. This operation makes the superposition calculation of pores non-attenuating, and the original pore phase is preserved.

Figure 8 presents the integrated digital rock of tight sandstone constructed by superposition method, whose voxel size is 400 × 400 × 400 and resolution is 0.25 μm/pixel.

3 Digital Rock Structure Characteristics

3.1 Connectivity Evaluation. The porosity ζ of digital rock is calculated by

$$\zeta = \frac{V_p}{V_p + V_s} \times 100 \tag{5}$$

where V_p is the volume of all pores (sum of connected pore volume and isolated pore volume), m^3. V_s is the solid volume, m^3. Here, we counted the number of voxels labeled 0 and voxels labeled 1 to calculate the pore volume and solid volume of digital rocks, respectively.

We evaluated the connectivity of digital rocks using the connected porosity, connected porosity ξ is defined by the following formula:

$$\xi = \frac{V'}{V_p + V_s} \times 100 \tag{6}$$

where, V' is the volume of connected pores, m^3.

The calculation results are shown in Table 1. We can see that the porosity of the integrated digital rock is slightly higher than that of the macro-pore digital rock and the micro-pore digital rock, and the connected porosity of the integrated digital rock is obviously higher than that of the other two digital rocks, which proves that the addition of micro-pores increases the pore connectivity of digital rock. Moreover, the porosity of integrated digital rock is higher than the measured porosity of real rock, while the connected porosity is close to the measured porosity; this is consistent with the fact that the rock porosity is measured with nitrogen in the laboratory, the isolated pores cannot be measured, and the measured porosity equals actually the connected porosity. As the strong heterogeneity of pore structure in tight sandstone, the single modeling method cannot capture all pore volume, and the integrated digital rock shows a better pore connectivity and good agreement with the real rock in connected porosity.

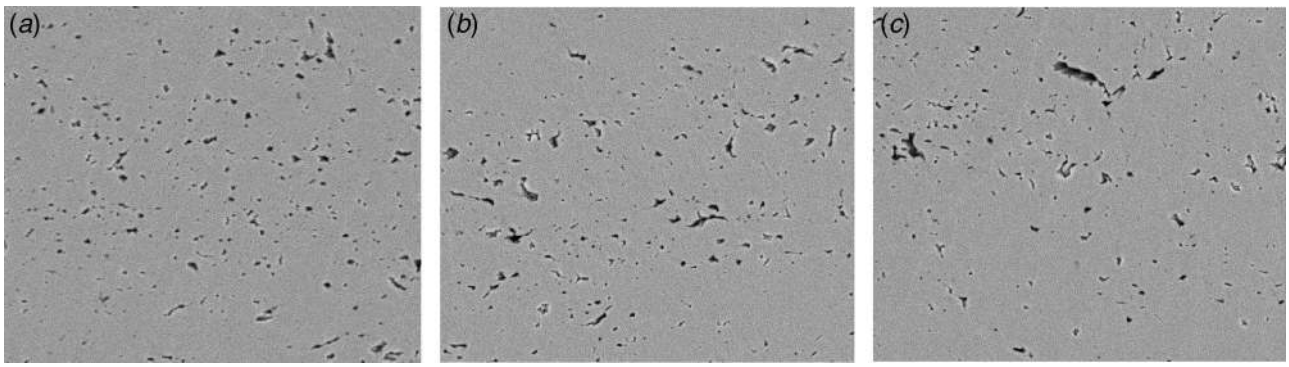

Fig. 4 SEM grayscale images of tight sandstone (700 × 600 pixels, light gray is solid, and dark gray is void): (*a*) XY plane, (*b*) XZ plane, and (*c*) YZ plane

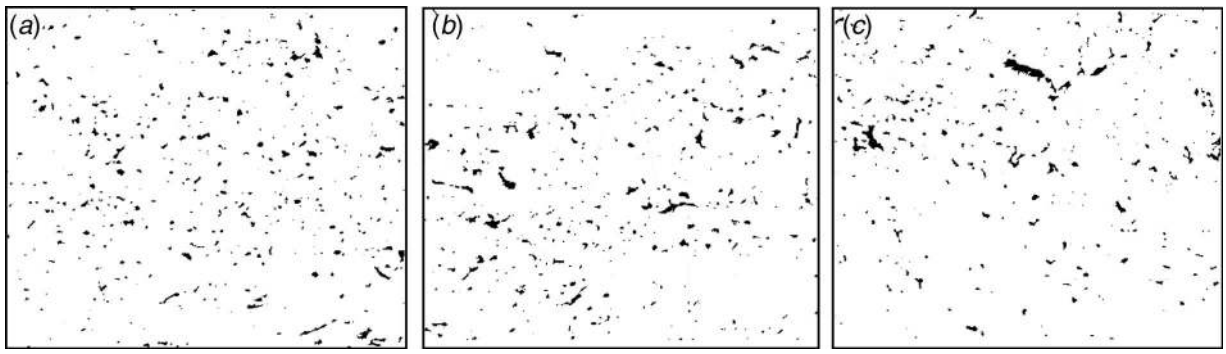

Fig. 5 Binary images of tight sandstone using SEM (700 × 600 pixels, white is solid, and black is void): (*a*) XY plane, (*b*) XZ plane, and (*c*) YZ plane

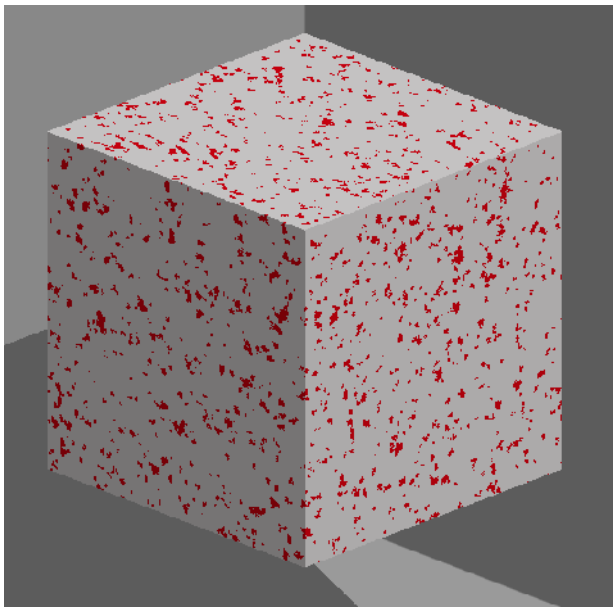

Fig. 6 3D micro-pore digital rock using MCMC (red is void and gray is solid) (Color version online.)

3.2 Pore-Throat Radius Distribution. At present, the main methods to build the topological pore network model of digital rock are multidirectional scanning method [50], medial axis approach [51], maximal ball algorithm [52], and Voronoi polyhedron method [53]. Among the above-mentioned methods, the maximal ball algorithm has the best effect in pore-throat division and recognition. This work used the maximal ball algorithm to extract the pore-throat parameters of digital rocks. Besides, the pore-throat parameters in the real rock was measured by the rate-controlled mercury intrusion [54,55], the tests were conducted with mercury-injection pressure of 0–1000 psi, mercury-injection speed of 0.00005 mL/min, contact angle of 140 deg, and interfacial tension factor of 485 dyn/cm.

We further compared the pore and throat radius distribution of digital rocks with that of the real rock in Fig. 9. Figure 9(*a*) shows that the pore radius of the real rock ranges from 3 μm to 43 μm, with a dominant radius of 7.5 μm. The distribution curve exhibits a single peak structure, which implies that the pore radius distribution of tight sandstone is relatively homogeneous. By comparing the digital rocks with the real rock, we can find that the pore radius distribution of integrated digital rock agrees best with that of real rock, followed by the micro-pore digital rock, and the pore radius distribution of macro-pore digital rock is wider. In general, the three digital rocks can capture and mimic pore information as well as adequate imaging resolution for pores in tight sandstone. From Fig. 9(*b*), we can see that there is a marked deviation between the digital rocks and the real rock. The throat radius distribution curve of real rock presents a single peak structure, and the throat radius ranges from 0.4 μm to 1.5 μm, with a dominant radius of 0.8 μm. However, the throat radius distribution of micro-pore digital rock and macro-pore digital rock is more concentrated and either smaller or larger, respectively, which may be due to imaging resolution limitation. In contrast, the integrated digital rock shows the best results with the smallest offset.

Through comparative analysis, we can find that the single-resolution imaging and single modeling method cannot reconstruct the pore-throat structure and recover the connectivity of tight sandstone digital rocks very well. A combination of X-ray CT and SEM enables us to capture micro-pores and macro-pores in an integrated model. Overall, the integrated digital rock exhibits good performance in modeling multi-scale void structures of tight sandstone.

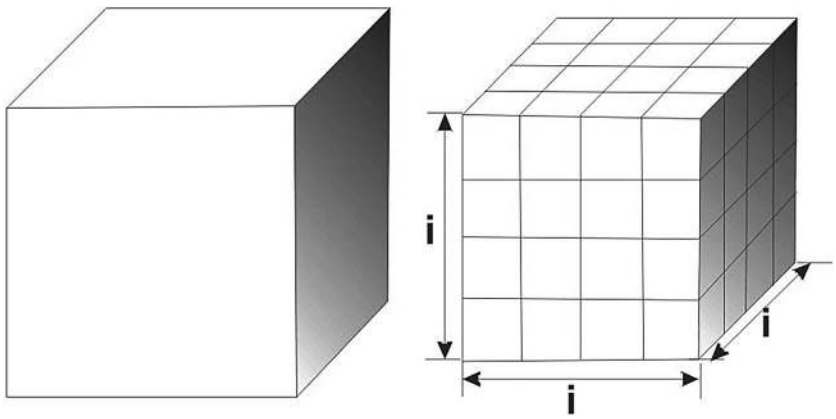

Fig. 7 Schematic diagram of voxel refinement

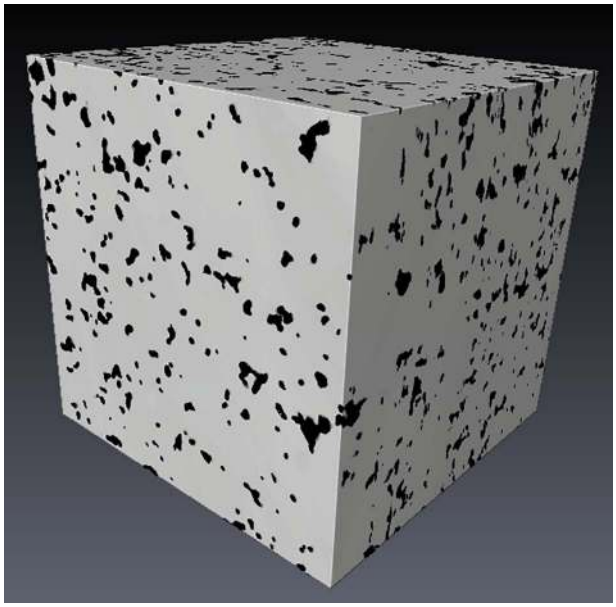

Fig. 8 Integrated digital rock of tight sandstone by the new method (gray is solid and black is void)

Table 1 Porosity comparison between digital rocks and real rock

Parameters	Macro-pore digital rock	Micro-pore digital rock	Integrated digital rock	Real rock
Porosity/%	15.02	14.39	16.93	–
Connected Porosity/%	11.23	12.79	14.53	14.75

4 Percolation Characteristics

The numerical simulations were completed with the Lattice-Boltzmann method (LBM) [56–58]. LBM can effectively simulate complex flows, such as porous media flow, suspension flow, multiphase flow, multicomponent flow, and so on. It is a mesoscopic method between the micro-molecular dynamics method and the macro-continuum hypothesis. The basic idea of this method is based on the theory of molecular dynamics, which obtains the macroscopic average characteristics by tracking the particle distribution function and finding the matrix of the distribution function. Here, the D3Q19 3D lattice-Boltzmann model was adopted, the lattice structure is shown in Fig. 10, and the velocity discrete Boltzmann-BGK equation is as follows:

$$f_i(r + e_i\delta_t, t + \delta_t) = f_i(r, t) - \frac{1}{\tau}[f_i(r, t) - f_{eqi}(r, t)] \tag{7}$$

where $f_i(r, t)$ is the distribution function of the particle in the i direction at t time and position $r(x, y, z)$, e_i is the velocity in the i direction, τ is the relaxation time, δ_t is the time step, and $f_{eqi}(r, t)$ is the equilibrium distribution function.

The discrete velocity direction is as follows:

$$e_i = \begin{cases} (0, 0, 0), i = 0; \\ (\pm 1, 0, 0), (0, \pm 1, 0), (0, 0, \pm 1), \\ i = 1, \ldots, 6; \\ (\pm 1, \pm 1, 0), (\pm 1, 0, \pm 1), (0, \pm 1, \pm 1), \\ i = 7, \ldots, 18 \end{cases} \tag{8}$$

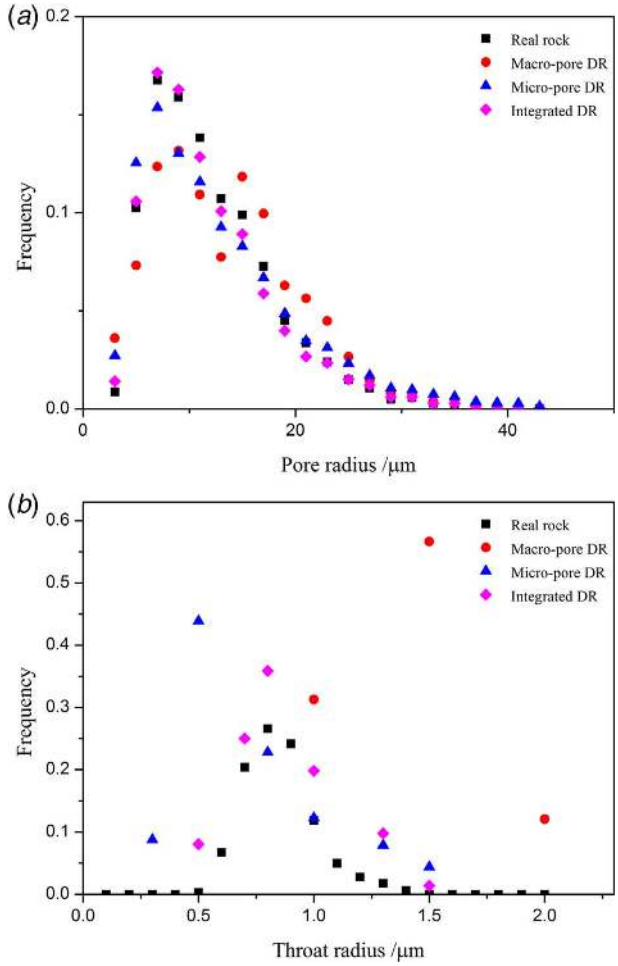

Fig. 9 Pore and throat radius distribution of digital rocks and real rock: (*a*) comparison of pore radius distribution between digital rocks and real rock and (*b*) comparison of throat radius distribution between digital rocks and real rock

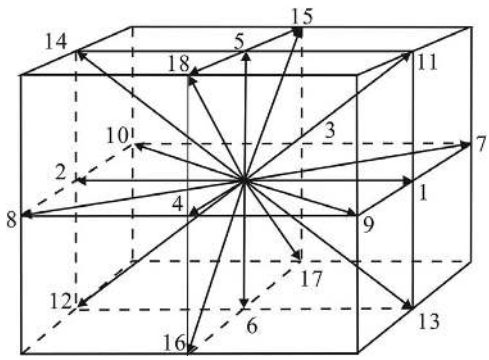

Fig. 10 D3Q19 lattice structure model

Equilibrium distribution function

$$f_{eqi}(r, t) = \rho\omega_i\left[1 + \frac{e_i u}{c_s^2} + \frac{(e_i u)^2}{2c_s^4} - \frac{u^3}{2c_s^2}\right] \tag{9}$$

where c_s is the lattice sound velocity, dimensionless, $c_s = 1/\sqrt{3}$; ω_i is the weight factor, $\omega_i = 1/3$, $i = 0$, $\omega_i = 1/18$, $i = 1, \ldots, 6$, $\omega_i = 1/36$, $i = 7, \ldots, 18$.

Local macro lattice density $\rho(r, t)$, lattice velocity $u(r, t)$, lattice pressure $p(r, t)$, and lattice viscosity $\mu(r, t)$ can be represented by

$$\rho(r, t) = \sum_i f_i(r, t), \quad p(r, t) = c_s^2 \rho(r, t),$$
$$u(r, t) = \frac{\sum_i f_i(r, t) e_i}{\rho(r, t)}, \quad \mu(r, t) = \frac{2\tau - 1}{6} \tag{10}$$

The inlet and outlet boundary is pressure boundary, the initial lattice velocity is 0, and the initial lattice density is 1. The permeability of digital rocks calculated by LBM is

$$k = -\mu(r, t)\phi \frac{\sum_{j=1}^{N} \sum_{i=0}^{n} f_i(r, t) e_i}{\sum_{j=1}^{N} \sum_{i=0}^{n} \Delta f_i(r, t) e_i} \tag{11}$$

where k is the lattice permeability, N is the total lattice number, and n is lattice direction, which is equal to 18.

$$\phi = \frac{N - \sum I(r)}{N}, \quad I(r) = \begin{cases} 0, & r(x, y, z) \text{ is void} \\ 1, & r(x, y, z) \text{ is solid} \end{cases} \tag{12}$$

The relationship between intrinsic permeability k_λ and lattice permeability k is

$$k_\lambda = kD^2 \tag{13}$$

where D is the lattice resolution, m.

We used the LBM to simulate the seepage process of macro-pore digital rock (Fig 3), micro-pore digital rock (Fig. 6) and integrated digital rock (Fig. 8) and obtained intrinsic permeability of digital rocks. The input pressure was 0.13 MPa and the output pressure was 0.1 MPa, the fluid viscosity was 0.018 mPa·s, and the velocity field is shown in Fig. 11. It is calculated that the intrinsic permeability of macro-pore digital rock is 0.126×10^{-3} μm^2, the permeability of micro-pore digital rock is 0.042×10^{-3} μm^2, and the permeability of integrated digital rock is 0.297×10^{-3} μm^2. The simulation results show that the permeability of integrated digital rock is greater than that of micro-pore digital rock and macro-pore digital rock, and imply micro-pores can improve conductivity greatly. In addition, the calculated permeability of integrated digital rock is in agreement with the experimental result, and it demonstrates that the integrated digital rock has similar infiltrability to real tight sandstone. The permeability ratio of integrated digital rock to macro-pore digital rock is 2.36; this indicates that micro-pores have great influence on permeability of digital rock model. Furthermore, we should fully consider and study the transport feature of pore-throats below 1 μ in tight sandstones.

5 Conclusion

In this paper, we introduced a new hybrid digital rock construction approach by combining X-ray CT method and Markov chain Monte Carlo (MCMC) method. Different from the hybrid numerical reconstruction methods, this hybrid method is the combination of physical experiments and numerical reconstruction. Compared with the micro-pores reconstructed using single SEM image by simulated annealing method (SAM), the micro-pores of integrated digital rock are reconstructed based on the three orthogonal surfaces of rock samples using MCMC, which can take into account more petrophysical information, such as heterogeneity and anisotropy. We have comparatively analyzed the structural and seepage characteristics of the integrated digital rock constructed by the new hybrid method, the macro-pore digital rock constructed by X-ray CT scanning method, and the micro-pore digital rock constructed by MCMC. It is concluded that the new hybrid method can better mimic synthetically the real rock, and the porosity and permeability of the integrated digital rock are basically consistent with that of the real rock. In addition, this study also shows that single-resolution imaging and separate modeling methods do not yield a satisfactory digital rock model, especially for tight sandstone with multi-scale pore-throat system. It is also worth mentioning that this new method possesses both the accuracy of the physical experiment methods and the convenience of the numerical reconstruction methods.

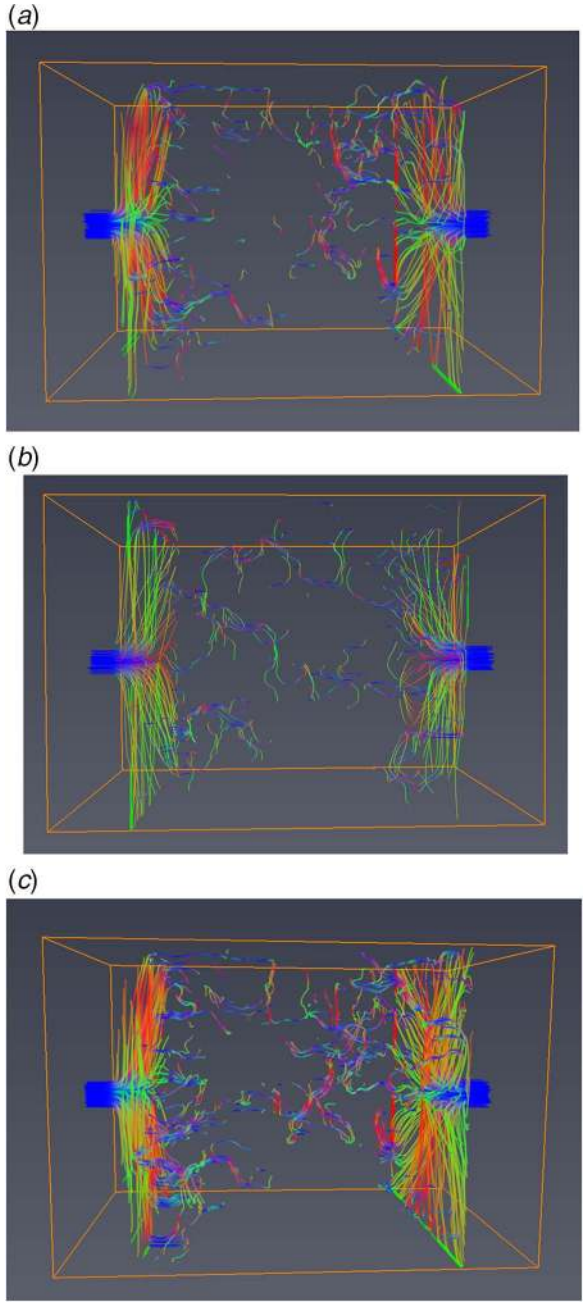

Fig. 11 Velocity field of digital rocks: (*a*) macro-pore digital rock (flow direction: left to right), (*b*) micropore digital rock (flow direction: left to right), and (*c*) integrated digital rock (flow direction: left to right)

Acknowledgment

The authors gratefully acknowledge financial support from the National Science and Technology Major Project of China (Grant No. 2017ZX05013-001), National Science and Technology Major Project of China (Grant No. 2017ZX05069-003), National Science Foundation (Grant No. 1724469), and also thank China Scholarship Council for funding Wei Lin. We want to thank the Department of Earth Science and Engineering, Imperial College London for sharing codes of the network extraction. In addition, the authors would like to recognize especially Professor Michael Manga and Dr. Xiaojing Fu for their revisions and comments on the introduction of the article.

References

[1] Scholl, M. A., and Harvey, R. W., 1992, "Laboratory Investigations on the Role of Sediment Surface and Groundwater Chemistry in Transport of Bacteria Through a Contaminated Sandy Aquifer," Environ. Sci. Technol., **26**(7), pp. 1410–1417.

[2] Saiers, J. E., and Hornberger, G. M., 1996, "The Role of Colloidal Kaolinite in the Transport of Cesium Through Laboratory Sand Columns," Water Resour. Res., **32**(1), pp. 33–41.

[3] Schrick, B., Hydutsky, B. W., Blough, J. L., and Mallouk, T. E., 2004, "Delivery Vehicles for Zerovalent Metal Nanoparticles in Soil and Groundwater," Chem. Mater., **16**(11), pp. 2187–2193.

[4] Yanagisawa, K., Nishioka, M., and Yamasaki, N., 1986, "Immobilization of Radioactive-Wastes in Hydrothermal Synthetic Rock," J. Nucl. Sci. Technol., **23**(6), pp. 550–558.

[5] Bateman, K., Turner, G., Pearce, J. M., Noy, D. J., Birchall, D., and Rochelle, C. A., 2005, "Large-Scale Column Experiment: Study of CO_2, Porewater, Rock Reactions and Model Test Case," Oil Gas Sci. Technol., **60**(1), pp. 161–175.

[6] Oloruntobi, O. S., and LaForce, T. C., 2009, "Effect of Aquifer Heterogeneity on CO_2 Sequestration," J. Soc. Pet. Eng., **21**.

[7] Xie, K., Lu, X. G., Li, Q., Jiang, W., and Yu, Q., 2016, "Analysis of Reservoir Applicability of Hydrophobically Associating Polymer," SPE J., **21**(1), pp. 1–9.

[8] Zhou, Y., Yin, D., Cao, R., and Zhang, C., 2018, "The Mechanism for Pore-Throat Scale Emulsion Displacing Residual Oil After Water Flooding," J. Petrol. Sci. Eng., **163**, pp. 519–525.

[9] Pereira, J. F. B., Costa, R., Foios, N., and Coutinho, J. A. P., 2014, "Ionic Liquid Enhanced Oil Recovery in Sand-Pack Columns," Fuel, **134**(15), pp. 196–200.

[10] Ghanbarian, B., Hamamoto, S., Kawamoto, K., Sakaki, T., Moldrup, P., Nishimura, T., and Komatsu, T., 2018, "Saturation-Dependent Gas Transport in Sand Packs: Experiments and Theoretical Applications," Adv. Water Resour., **122**, pp. 139–147.

[11] Fredrich, J. T., Menendez, B., and Wong, T. F., 1995, "Imaging the Pore Structure of Geomaterials," Science, **268**(5208), pp. 276–279.

[12] Yin, X., Zheng, Y., and Zong, Z., 2017, "Research on the Equivalence Between Digital Core and Rock Physics Models," J. Geophys. Eng., **14**(3), pp. 666–674.

[13] Han, X.H., Yang, L., Hou, Q.Y., Li, F.B., and Wang, H.L., 2013, "A New Method for Making Artificial Rock of Unconsolidated Sandstone Cemented by Dispersed Shale," Prog. Geophys., **28**(6), pp. 2944–2949.

[14] Alhashmi, Z., Blunt, M. J., and Bijeljic, B., 2016, "The Impact of Pore Structure Heterogeneity, Transport, and Reaction Conditions on Fluid-Fluid Reaction Rate Studied on Images of Pore Space," Transport Porous Med., **115**(2), pp. 215–237.

[15] Lin, Q., Al-Khulaifi, Y., Blunt, M. J., and Bijeljic, B., 2016, "Quantification of Sub-Resolution Porosity in Carbonate Rocks by Applying High-Salinity Contrast Brine Using X-Ray Microtomography Differential Imaging," Adv. Water Resour., **96**, pp. 306–322.

[16] Iglauer, S., Paluszny, A., and Blunt, M. J., 2013, "Simultaneous Oil Recovery and Residual Gas Storage: A Pore-Level Analysis Using in Situ X-Ray Micro-Tomography," Fuel, **103**, pp. 905–914.

[17] Tomutsa, L., Silin, D., and Radmilovic, V., 2007, "Analysis of Chalk Petrophysical Properties by Means of Submicron-Scale Pore Imaging and Modeling," SPE Reservoir Eval. Eng., **10**(3), pp. 285–293.

[18] Paddock, S. W., 2000, "Principles and Practices of Laser Scanning Confocal Microscopy," Mol. Biotechnol., **16**(2), pp. 127–149.

[19] Izadi, H., Baniassadi, M., Hasanabadi, A., Mehrgini, B., Memarian, H., Soltanian-Zadeh, H., and Abrinia, K., 2017, "Application of Full Set of Two Point Correlation Functions From a Pair of 2D Cut Sections for 3D Porous Media Reconstruction," J. Petrol. Sci. Eng., **149**, pp. 789–800.

[20] Befus K, S., and Manga, M., 2019, "Supereruption Quartz Crystals and the Hollow Reentrants," Geology, **47**(8), pp. 710–714.

[21] Lin, W., Li, X., Yang, Z., Manga, M., Fu, X., Xiong, S., Gong, A., Chen, G., Li, H., Pei, L., Li, S., Zhao, X., and Wang, X., 2019, "Multiscale Digital Porous Rock Reconstruction Using Template Matching," Water Resour. Res., **55**(8), pp. 6911–6922.

[22] Shen, W. J., Song, F. Q., Hu, X., Zhu, G., and Zhu, W., 2019, "Experimental Study on Flow Characteristics of Gas Transport in Micro- and Nanoscale Pores," Sci. Rep., **9**(1), p. 10196.

[23] Li, Y. X., Hu, Z. M., Liu, X. G., Duan, X., Gao, S., Wang, W., and Chang, J., 2019, "Pressure-Dependent Equilibrium Molecular Simulation of Shale Gas and Its Distribution and Motion Characteristics in Organic–Rich Nano-Slit," Fuel, **237**, pp. 1040–1049.

[24] Li, Y. X., Hu, Z. M., Liu, X. G., Gao, S., Duan, X., Chang, J., and Wu, J., 2018, "Insights Into Interactions and Microscopic Behavior of Shale Gas in Organic-Rich Nano-Slits by Molecular Simulation," J. Nat. Gas Sci. Eng., **59**, pp. 309–325.

[25] Quiblier, J. A., 1984, "A new Three-Dimensional Modeling Technique for Studying Porous Media," J. Colloid Interface Sci., **98**(1), pp. 84–102.

[26] Hazlett, R. D., 1995, "Simulation of Capillary-Dominated Displacements in Microtomographic Images of Reservoir Rocks," Transport Porous Med., **20**(1–2), pp. 21–35.

[27] Karsanina, M. V., Gerke, K. M., Skvortsova, E. B., Mallants, D., and Guda, T., 2015, "Universal Spatial Correlation Functions for Describing and Reconstructing Soil Microstructure," PLoS One, **10**(5), p. e0126515.

[28] Okabe, H., and Blunt, M. J., 2004, "Prediction of Permeability for Porous Media Reconstructed Using Multiple-Point Statistics," Phys. Rev. E, **70**(6), p. 066135.

[29] Tahmasebi, P., Hezarkhani, A., and Sahimi, M., 2012, "Multiple-Point Geostatistical Modeling Based on the Cross-Correlation Functions," Comput. Geosci., **16**(3), pp. 779–797.

[30] Zhang, N., Sun, Q., Fadlelmula, M., Rahman, A., and Wang, Y., 2018, "A New Method of Porous Space Reconstruction Using Multipoint Histogram Technology," ASME J. Energy Resour. Technol., **140**(3), p. 032909.

[31] Keehm, Y., Mukerji, T., and Nur, A., 2004, "Permeability Prediction From Thin Sections: 3D Reconstruction and Lattice-Boltzmann Flow Simulation," Geophys. Res. Lett., **31**(4), p. L04606.

[32] Wu, K. J., Nunan, N., Crawford, J. W., Young, I. M., and Ritz, K., 2004, "An Efficient Markov Chain Model for the Simulation of Heterogeneous Soil Structure," Soil Sci. Soc. Am. J., **68**(2), pp. 346–351.

[33] Ning, Z. P., Zhang, L. X., and Zheng, W. X., 2019, "Observer-Based Stabilization of Nonhomogeneous Semi-Markov Jump Linear Systems With Mode-Switching Delays," IEEE Trans. Autom. Control, **64**(5), pp. 2029–2036.

[34] Ning, Z. P., Zhang, L. X., and Colaneri, P., 2019, "Semi-Markov Jump Linear Systems With Incomplete Sojourn and Transition Information: Analysis and Synthesis," IEEE Trans. Autom. Control,

[35] Zhang, L. X., Ning, Z. P., and Shi, P., 2015, "Input-Output Approach to Control for Fuzzy Markov Jump Systems With Time-Varying Delays and Uncertain Packet Dropout Rate," IEEE Trans. Cybernetics, **45**(11), pp. 2449–2460.

[36] Bryant, S., and Blunt, M. J., 1992, "Prediction of Relative Permeability in Simple Porous Media," Phys. Rev. A, **46**(4), pp. 2004–2011.

[37] Oren, P. E., and Bakke, S., 2002, "Process Based Reconstruction of Sandstones and Prediction of Transport Properties," Transport Porous Med., **46**(2–3), pp. 311–343.

[38] Talukdar, M. S., and Torsaeter, O., 2002, "Reconstruction of Chalk Pore Networks From 2D Backscatter Electron Micrographs Using a Simulated Annealing Technique," J. Petrol. Sci. Eng., **33**(4), pp. 265–282.

[39] Politis, M. G., Kikkinides, E. S., Kainourgiakis, M. E., and Stubos, A. K., 2008, "A Hybrid Process-Based and Stochastic Reconstruction Method of Porous Media," Microporous Mesoporous Mater., **110**(1), pp. 92–99.

[40] Liu, X., Sun, J., and Wang, H., 2009, "Reconstruction of 3-D Digital Cores Using a Hybrid Method," Appl. Geophys., **6**(2), pp. 105–112.

[41] Lin, W., Li, X. Z., Yang, Z. M., Wang, J., Xiong, S., Luo, Y., and Wu, G., 2017, "Construction of Dual Pore 3-D Digital Cores With a Hybrid Method Combined With Physical Experiment Method and Numerical Reconstruction Method," Transport Porous Med., **120**(1), pp. 227–238.

[42] Yang, Z. M., Ma, Z. Z., Luo, Y. T., Zhang, Y.P., Guo, H.K., and Lin, W., 2018, "A Measured Method for In Situ Viscosity of Fluid in Porous Media by Nuclear Magnetic Resonance," Geofluids, **2018**, p. 9542152.

[43] Chen, T., Yang, Z. M., Luo, Y. T., Lin, W., Xu, J., Ding, Y., and Niu, J., 2018, "Evaluation of Displacement Effects of Different Injection Media in Tight Oil Sandstone by Online Nuclear Magnetic Resonance," Energies, **11**(10), p. 2836.

[44] Zhao, X. L., Yang, Z. M., Lin, W., Xiong, S.C., Luo, Y.T., Wang, Z.Y., Chen, T., Xia, D.B., and Wu, Z.K., 2019, "Study on Pore Structures of Tight Sandstone Reservoirs Based on Nitrogen Adsorption, High-Pressure Mercury Intrusion, and Rate-Controlled Mercury Intrusion," ASME J. Energy Resour. Technol., **141**(11), p. 112903.

[45] Xiao, Q. H., Fang, F. F., Wang, Z. Y., Jiang, B., and Yuan, Y., 2019, "Nuclear Magnetic Resonance Simulation Experiment for a Water Drive Gas Reservoir," ASME J. Energy Resour. Technol., **141**(11), p. 112901.

[46] Perez, A., and Gonzalez, R. C., 1987, "An Iterative Thresholding Algorithm for Image Segmentation," IEEE Trans. Pattern Anal. Mach. Intell., **9**(6), pp. 742–751.

[47] Otsu, N., 1979, "A Threshold Selection Method From Gray-Level Histogram," IEEE Trans. Syst. Man Cybernetics, **9**(1), pp. 62–66.

[48] Kittler, J., Illing, W. J., and Foglein, J., 1985, "Threshold Selection Based on a Simple Image Static," Comput. Vis. Graph. and Image Process., **30**(2), pp. 125–147.

[49] Lin, W., Li, X. Z., Yang, Z. M., Lin, L., Xiong, S., Wang, Z., Wang, X., and Xiao, Q., 2018, "A New Improved Threshold Segmentation Method for Scanning Images of Reservoir Rocks Considering Pore Fractal Characteristics," Fractals, **26**(2), p. 1840003.

[50] Zhao, H. Q., Macdonald, I. F., and Kwiecien, M. J., 1994, "Multi-Orientation Scanning: A Necessity in the Identification of Pore Necks in Porous Media by 3-D Computer Reconstruction From Serial Section Data," J. Colloid Interface Sci., **162**(2), pp. 390–401.

[51] Lindquist, W. B., and Venkatarangan, A., 1999, "Investigating 3D Geometry of Porous Media From High Resolution Images," Phys. Chem. Earth, Part A, **24**(7), pp. 593–599.

[52] Al-Kharusi, A. S., and Blunt, M. J., 2007, "Network Extraction From Sandstone and Carbonate Pore Space Images," J. Petrol. Sci. Eng., **56**(4), pp. 219–231.

[53] Bryant, S. L., King, P. R., and Mellor, D. W., 1993, "Network Model Evaluation of Permeability and Spatial Correlation in a Real Random Sphere Packing," Transport Porous Med., **11**(1), pp. 53–70.

[54] Zhao, X. L., Yang, Z. M., Lin, W., Xiong, S., and Wei, Y., 2018, "Characteristics of Microscopic Pore-Throat Structure of Tight oil Reservoirs in Sichuan Basin Measured by Rate-Controlled Mercury Injection," Open Phys., **16**(1), pp. 675–684.

[55] Zhao, X. L., Yang, Z. M., Lin, W., Xiong, S.C., Luo, Y.T., Liu, X.W., and Xia, D.B., 2019, "Fractal Study on Pore Structure of Tight Sandstone Based on Full-Scale map," Int. J. Oil Gas Coal Technol., **22**(2), p. 123.

[56] Zhao, W. D., Zhang, Y., Xu, B., Li, P., Wang, Z., and Jiang, S., 2018, "Multiple-Relaxation-Time Lattice Boltzmann Simulation of Flow and Heat Transfer in Porous Volumetric Solar Receivers," ASME J. Energy Resour. Technol., **140**(8), p. 082003.

[57] Ma, X. F., Mou, J. Y., Lin, H., Jiang, F., Liu, K.Y., and Zhao, X.Z., 2017, "Lattice Boltzmann Simulation of Wormhole Propagation in Carbonate Acidizing," ASME J. Energy Resour. Technol., **139**(4), p. 042002.

[58] Chen, S. Y., Wang, Z., Shan, X. W., and Doolen, G. D., 1992, "Lattice Boltzmann Computational Fluid-Dynamics in 3 Dimensions," J. Stat. Phys., **68**(3–4), pp. 379–400.